IEEE Access
The journal for rapid open access publishing

Received December 14, 2014, accepted January 29, 2015, date of publication February 11, 2015,
date of current version February 23, 2015.

Digital Object Identifier 10.1109/ACCESS.2015.2402673

Performance Evaluation of *a Priori* Information on Reconstruction of Fluorescence Molecular Tomography

XIN LIU[1], (Member, IEEE), ZHUANGZHI YAN[1], AND HONGBING LU[2], (Member, IEEE)
[1]School of Communication and Information Engineering, Shanghai University, Shanghai 200444, China
[2]Department of Biomedical Engineering, Fourth Military Medical University, Xi'an 710032, China

Corresponding author: H. Lu (luhb@fmmu.edu.cn)

This work was supported in part by the Shaanxi Natural Science Foundation under Grant 2013JM4008 and in part by the National Natural Science Foundation of China under Grant 81371604, Grant 81230035, and Grant 61372046.

ABSTRACT Fluorescence molecular tomography (FMT) plays an important role in *in vivo* small animal imaging. However, due to the diffusive nature of photon propagation in biological tissues, FMT suffers from a low spatial resolution, which limits its capability of resolving the distribution of fluorescent biomarkers. In this paper, we investigate the effect of functional and structural *a priori* information on the accuracy of FMT reconstruction by a hybrid FMT and X-ray computed tomography imaging system. The results from numerical simulation and phantom experiments suggest that the fluorescence targets embedded in heterogeneous medium can be localized when structural *a priori* information is utilized to constrain the reconstruction process. In addition, both the functional and structural *a priori* information are essential for the recovery of fluorophore concentration.

INDEX TERMS Image reconstruction, optical imaging, reconstruction algorithms.

I. INTRODUCTION

Interest in visualizing fluorescent bio-markers in small animals and humans *in vivo* has led to the rapid development of optical imaging technique, such as fluorescence molecular tomography (FMT) [1], [2]. Compared with planar fluorescence reflectance imaging [3], FMT uses physical model of light propagation in diffuse tissue and allows reconstructing three-dimensional (3-D) distribution of fluorophore in living subjects [1], [2]. With the development of optical probes [3], [4], imaging systems [5]–[7], and reconstruction algorithms [8]–[20], this new technology has been successfully applied to basic medical diagnosis [21]–[23] and drug delivery research [24].

Despite these advances, FMT, as an imaging technique based on diffusive light, suffers from a low spatial resolution for two main reasons. First, photon field propagating in biological tissues is highly scattering, which results in a highly ill-posed reconstruction problem compared to anatomical imaging, e.g., x-ray computed tomography (XCT) or magnetic resonance imaging (MRI). Second, the structure information and optical properties of the imaged object are difficult to be accurately acquired by optical imaging system alone. As a result, the mathematical model (forward model) used to describe the photon migration inside imaged object is approximate, which further challenges the imaging problem.

To overcome these limitations, several attempts have been made [8]–[16]. It has been reported that *structural a priori* information (anatomical structure), available from XCT or MRI, is effective in guiding and constraining the reconstruction process of FMT. By applying *structural a priori* information into FMT processes (e.g., using the Laplace regularization [7], [12], the Helmholtz regularization [13], the weighed segments regularization [8], or the Laplace with weighed segments regularization [5], [9]), the reconstruction quality of FMT can be improved. Besides, in optical tomography, the distribution of fluorophore is computed by minimizing the misfit between the experimental measurements and the measurements predicated by forward model. Hence the reconstruction accuracy of FMT can also be improved if a appropriate *functional a priori* information is taken into account [11], [14], [15]. Here, *functional a priori* information is defined as the optical properties (absorption coefficient and scattering coefficient) of the tissues/medium,

which are used to compute the accurate forward model. Further, by using *functional a priori* information combined with *structural a priori* information, Lin *et al.* quantitatively recovered the fluorophore's concentration within the imaged object [11]. In their work, the optical properties were explicitly acquired by diffuse optical tomography (DOT). With DOT technique, theoretically, we could obtain the accurate optical properties. However, the method increased the experimental complexity and required the additional computation burden. As a result, there was a tradeoff between the reconstruction quality and the experimental complexity. So, it was interesting to investigate whether the use of the approximate optical properties (e.g., the lookup-table optical property) was enough to recover the fluorescent distributions, combined with *structural a priori* information. To address the problem, Hyde *et al.* evaluated the effect of the optical properties on the FMT reconstruction [10], where they compared the reconstruction performance of FMT obtained by the different optical properties. However, we should note that the conclusion was obtained only by the numerical simulation studies and was not further supported by the experiments. In addition, as Hyde *et al.* pointed out, in the reconstruction processes, *structural a priori* information was used in a very simple method.

Hence, it is necessary to experimentally evaluate the roles of *a priori* information in FMT reconstruction. In other words, the systemic experimental studies should be performed to understand whether the use of more accurate optical properties is necessary when *structural a priori information* is taken into account, or what degree *structural a priori* information can compensate for approximation of the optical properties. The study will help us in better understanding which kind of experimental strategies is more appropriate for the use of *a priori* information in FMT reconstruction.

To address the problem, in this paper, we analyze and compare the effect of *a priori* information, including *structural a priori* information (anatomical structure) and *functional a priori* information (optical properties of media/tissues), on FMT reconstruction accuracy. First, we evaluate the effect of *structural a priori* information on FMT reconstruction, incorporating accurate optical properties. In the case, the Laplace regularization and the Laplace with weighted segments regularization, as structural regularization term, are used to guide and constrain FMT reconstruction processes. Second, based on the mismatch and homogeneous optical properties (*functional a priori* information), we construct the forward models and evaluate their influences on FMT reconstruction accuracy, where the Laplace with weighted segment regularization is used in inverse problem of FMT. The experimental results from numerical simulation and phantom experiment suggest that when *structural a priori* information is utilized to guide and constrain reconstruction process, the fluorescence targets embedded in heterogeneous medium can be clearly localized, even if there are great variances in the optical properties. In addition, both *functional and structural a priori* information are essential for the recovery of the fluorophore concentration. When the *structural a priori* information is applied alone or incorporating the mismatched *functional a priori* information, the fluorophore concentration cannot be accurately recovered.

The paper is organized as follows. In Section II, the methods used are detailed, including the forward model, inverse problem, and *functional and structural a priori* information. In Section III, the experimental materials are described. The experimental results are shown in Section IV. Finally, we discuss the results and draw conclusions in Section V.

II. METHODS

A. FORWARD MODEL

In highly scattering tissue media, the photon migration can be modeled using the diffusion approximation to the radiative transport equation. For the continuous wave (CW) mode, the Green's function $G(r)$ describing the light transportation due to a point excitation source $\delta(r - r_s)$ can be obtained by solving the following diffusion equation

$$-\nabla \cdot [D(r)\nabla G(r)] + \mu_a(r)G(r) = \delta(r - r_s) \quad r \in \Omega \tag{1}$$

with the Robin-type boundary condition

$$2\rho D(r)\frac{\partial G(r)}{\partial \vec{n}} + G(r) = 0 \quad r \in \partial\Omega \tag{2}$$

where Ω is the domain of the imaged object and $\partial\Omega$ is the boundary; $\mu_a(r)$ is the absorption coefficient and $D(r)$ is the diffusion coefficient of the tissue at position r; $\vec{n}$ denotes the outward normal vector to the boundary $\partial\Omega$, and ρ is a constant depending upon the optical reflective index mismatch at the boundary [19]. A collimated point source spot can be modeled as an isotropic source $\delta(r - r_s)$, which is one transport mean free path $ltr = 1/\mu_s'$ beneath the illumination surface. With the known optical properties, the Green's function can be obtained by solving Eq. (1) using the finite element method [20]. After obtaining these Green's functions, the fluorescence signal, due to an excitation source at r_s and a detector at r_d, can be expressed by the first order Born approximation [18]

$$\Phi_m(r_d, r_s) = \int_V G^{\lambda_{fl}}(r_d, r_p)n(r_p)G^{\lambda_{exc}}(r_p, r_s)dr_p \tag{3}$$

where r_p is the point inside the volume V considered for reconstruction; $n(r_p)$ denotes the fluorescence yield at point r_p; the Green's function $G^{\lambda_{fl}}(r_d, r_p)$ describes the light propagating from r_p to the position of detector r_d at the fluorescence/emission wavelength; the Green's function $G^{\lambda_{exc}}(r_p, r_s)$ describes the light propagating from the position of source r_s to r_p at the excitation wavelength. To eliminate the effect of source intensities and detector sensitivities in the experiments, in this paper, the normalized born approximation is used [17]. The normalized born ratio $U_m(r_d, r_s)/U_x(r_d, r_s)$ of the measured fluorescence signal over the corresponding excitation signal is

expressed as follows

$$\frac{U_m(r_d, r_s)}{U_x(r_d, r_s)} = \Theta \frac{\int_V G^{\lambda_{fl}}(r_d, r_p) n(r_p) G^{\lambda_{exc}}(r_p, r_s) dr_p}{G^{\lambda_{exc}}(r_d, r_s)} \tag{4}$$

where the Green's function $G^{\lambda_{exc}}(r_d, r_s)$ describes the light propagating from r_s to r_d at the excitation wavelength; Θ is a calibration parameter which accounts for the unknown gain and attenuation factors of the system. When the volume V is sampled on a 3-D grid, Eq. (4) is described as follows

$$\frac{U_m(r_d, r_s)}{U_x(r_d, r_s)} = \Theta \sum_{p=1}^{N} \frac{G^{\lambda_{fl}}(r_d, r_p) n(r_p) G^{\lambda_{exc}}(r_p, r_s)}{G^{\lambda_{exc}}(r_d, r_s)} \Delta V(r_p) \tag{5}$$

where $\Delta V(r_p)$ is the volume of the discretized voxel centered at r_p and N is the total number of the discretized voxels. For all source-detector pairs, the forward model can be written as a linear system

$$u = \mathbf{W} n \tag{6}$$

where $\mathbf{W}$, with a size of $N_{data} \times N_{voxels}$, is the weight matrix. N_{data} is the total number of all source-detector pairs and N_{voxels} is the total number of voxels.

B. INVERSE PROBLEM

Generally, the weight matrix $\mathbf{W}$ is poorly conditioned, making direct inversion impossible. An estimation of the fluorophore distribution can be found by least-squares minimization of the difference between the measured fluorescence signal u and the fluorescence signal $\hat{u}$, predicted by the forward model $\hat{u} = \mathbf{W}\hat{n}$ with $\hat{n}$ being the estimated fluorophore's concentration. The objective function Q to be minimized is given as follows

$$Q = \left\| \mathbf{W}\hat{n} - u \right\|^2 + \lambda^2 \left\| L\hat{n} \right\|^2 \tag{7}$$

where λ is the regularization parameter used to control the degree of regularization, and its value is determined by the L-curve analysis [25]; $\mathbf{L}$ is the regularization matrix, which is used to stabilize the problem. The most common type of regularization is the Tikhonov regularization, with $\mathbf{L} = \mathbf{I}$, leading to

$$Q = \left\| \mathbf{W}\hat{n} - u \right\|^2 + \lambda^2 \left\| \hat{n} \right\|^2 \tag{8}$$

For standard Tikhonov regularization, the minimization of Eq. (8) can be solved using a least-squares algorithm (LSQR) [26]. For the more general problem, if the regularization matrix $\mathbf{L}$ is invertible, Eq. (7) can be transformed to standard form by substituting $\hat{n} = \mathbf{L}^{-1}\bar{n}$

$$Q = \left\| \mathbf{W}\mathbf{L}^{-1}\bar{n} - u \right\|^2 + \lambda^2 \left\| \bar{n} \right\|^2 \tag{9}$$

The minimization of Eq. (9) yields a result for $\bar{n}$, which can then be transformed back to $\hat{n}$ by $\hat{n} = \mathbf{L}^{-1}\bar{n}$.

C. STRUCTURAL A PRIORI INFORMATION

The *structural a prior* information (anatomical structure), available from XCT or MRI, can be included in the inverse problem by shaping the regularization matrix $\mathbf{L}$. Here, two different types of regularization are used: (i) the Laplace regularization and (ii) the Laplace with weighted segments regularization.

1) LAPLACE REGULARIZATION

The Laplace regularization is a method derived from the Laplace equation. This method smoothes the solution within individual segments, while allowing discontinuities across segment borders. According to [12] and [13], the regularization matrix is given as follows

$$L_{ij} = \begin{cases} -\frac{1}{N_m}, & \text{if } i \text{ and } j \text{ in the same region } m \\ 1, & \text{if } i = j \\ 0, & \text{otherwise} \end{cases} \tag{10}$$

where N_m is the total number of voxels in segment m.

2) LAPLACE WITH WEIGHTED SEGMENTS REGULARIZATION

Generally, XCT image has a higher resolution than FMT. Hence in tissue boundaries, each FMT voxel may occupy more than one anatomic region. To apply anatomical information in the inverse problem more accuracy, in this paper, the Laplace with weighted segments regularization is used [8], [9]. The corresponding regularization matrix is given as follows

$$L_{ij} = \begin{cases} -a_i \sum_{m=1}^{M} \frac{c_{im} c_{jm}}{N_m}, & \text{if } i \text{ and } j \text{ in the same region} \\ a_i \sum_{m=1}^{M} c_{im}, & \text{if } i = j \\ 0, & \text{otherwise} \end{cases} \tag{11}$$

where N_m is the total number of voxels in region m; c_{im} is the volume percentage of voxel i that is contained in region m; a_i is the voxel weight, which is determined in a data driven way without user intervention [8]. The derivation of a_i is detailed in the Appendix. After obtaining the corresponding regularization matrix, the minimization of Eq. (9) is performed by LSQR [26].

D. FUNCTIONAL A PRIORI INFORMATION

In optical tomography, the reconstruction accuracy of FMT can be further improved if *functional a priori* information is taken into account [11], [14], [15]. Based on this consideration, in this paper, we also investigate the effect of *functional a priori* information on reconstruction accuracy of FMT. Here, *functional a priori* information is defined as the optical properties of heterogeneous medium, which are used to compute forward model. In detail, to construct the heterogeneous forward model, the XCT data are first segmented into a number of the individual organs/tissues. Then, the appropriate absorption and scattering coefficients are

assigned to each segmented anatomical regions, respectively. Finally, the heterogeneous forward model is generated by solving the diffusion equation with the finite element method (COMSOL Multiphysics 3.3, COMSOL, Inc., Burlington, MA, USA).

E. ERROR ANALYSIS

To better evaluate the effect of different optical properties (forward models) on FMT reconstruction accuracy, in the paper, the relative error is used and defined as follows

$$RelativeError = 100\sqrt{\sum_i \left(\frac{x_i^{mismatch} - x_i^{accurate}}{x_i^{accurate}}\right)^2} \quad (12)$$

where $x_i^{mismacth}$ is the reconstructed fluorophore concentration at pixel i obtained by the mismatched optical properties and $x_i^{accurate}$ is the reconstructed fluorophore concentration at pixel i obtained by the accurate optical properties.

III. MATERIALS

A. FMT/MICRO-XCT IMAGING SYSTEM

Experiments were performed with a hybrid FMT/XCT imaging system previously developed by our laboratory [5]. The sketch of the system is shown in Fig. 1.

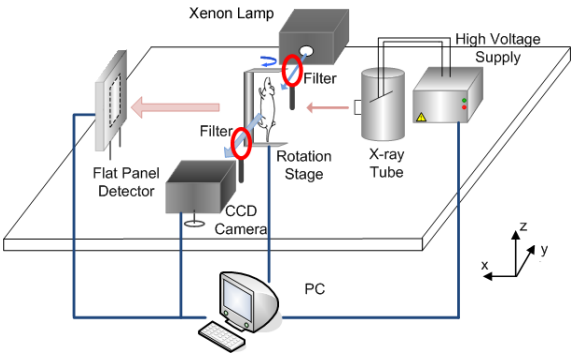

FIGURE 1. The hybrid FMT/micro-XCT imaging system.

Briefly, the imaged object was placed on a custom-built rotating stage which allowed rotation and shifting of the target. For optical imaging, the small light spot from a 300W Xenon lamp (Asahi Spectra, Torrance, CA, USA) traveled through a 780 ± 5nm band pass filter (Asahi Spectra, Torrance, CA, USA) to provide the excitation light. The photons propagating through the imaged object were detected by a 14-bit electron multiplying charge coupled device (EMCCD) camera (Andor, Belfast, Northern Ireland), coupled with a 35 mm, F1.6 lens (Pentax, Tokyo, Japan). Around the rotational stage, a micro-XCT system was constructed by an x-ray source (Oxford Instrument, CA, USA), a CMOS flat panel detector (Hamamatsu, Shizuoka, Japan), and a host PC equipped with a PCI-1422 frame grabber.

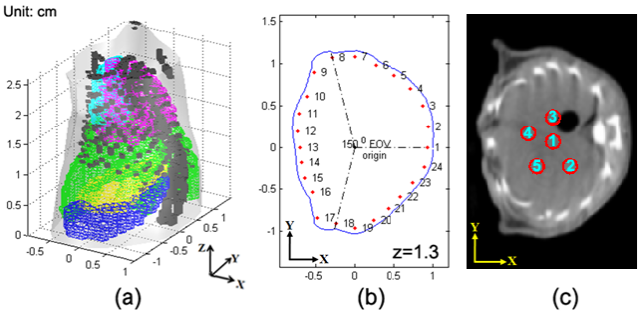

FIGURE 2. Schematic diagram of simulation study. (a) The 3-D mouse geometry model used in the numerical simulation with a length of 2.6 cm from the neck to the base of the liver. The actual boundaries of different organs are depicted with different colors (surface: gray; heart: cyan; lung: magenta; liver: green; spleen: blue; stomach: yellow; bones: black). (b) The plane of excitation sources at z=1.3 cm. In this paper, 360° full angle fluorescence tomography is performed with 24 projections in 15° step. The red points 1-24 in (b) depict the discrete excitation sources for the 24 projections. For each excitation location, fluorescence measurements are acquired from the opposite side within 150° field of view. (c) The locations of five fluorescence inclusions in the liver.

B. NUMERICAL SIMULATION

In the numerical simulation, a virtual mouse atlas was used to provide 3-D anatomical information [27], which could be downloaded from http://neuroimage.usc.edu/Digimouse.html. Here, we selected the mouse torso from the neck to the base of the liver [see Fig. 2(a)] as the investigated region, which is a challenging region for optical reconstruction due to the presence of the highly scattering lung and the highly absorbing liver. The optical properties (absorption and scattering coefficients) from [28] (see Table 1) were assigned to corresponding anatomical regions to simulate photons propagation in heterogeneous tissues. The optical properties outside of these tissues were regarded as homogeneous.

TABLE 1. Optical properties of tissues in mouse at 700-800 nm [28].

Tissue type	μ_a (cm^{-1})	μ_s' (cm^{-1})
Heart	0.156	9.0
Liver	0.935	6.4
Lung	0.516	21.2
Spleen	0.935	6.4
Stomach	0.0296	13.7
Bones	0.161	23.2

To evaluate the effect of *structural a priori* information (anatomical structure) and *functional a priori* information (optical properties of media/tissues) on the reconstruction accuracy, five fluorescence targets (approximately 1.6 mm in diameter, 3 mm in height) were embedded at a non-overlapping location within the liver [see Fig. 2(c)]. Additionally, 10% Gaussian noise was added to the synthetic measurement data to simulate the actual case.

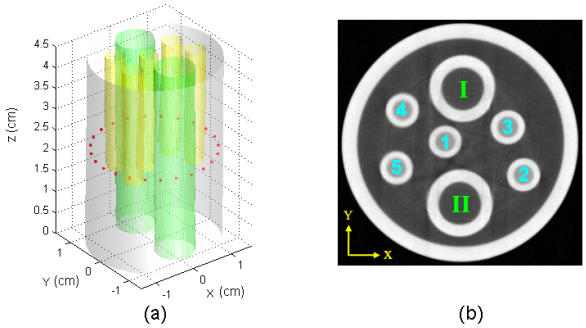

FIGURE 3. Schematic diagram of phantom experiment. (a) The 3-D view of the phantom. (b) The top view of the phantom. Two cylinders (outer diameter ∼8.5 mm) are placed into a larger cylinder (outer diameter ∼3 cm) to produce the heterogeneous phantom. The background optical properties are $\mu_a = 0.3\ \text{cm}^{-1}$ and $\mu_s' = 10.0\text{cm}^{-1}$. The optical properties for the two 8.5 mm diameter cylinders [the two green cylinders in (a)] are $\mu_a = 1.0\ \text{cm}^{-1}$ and $\mu_s' = 10.0\ \text{cm}^{-1}$. Five glass tubes [outer diameter ∼4.5 mm, the yellow cylinders in (a)] filled with 1 μM ICG solution are placed inside the cylinder phantom, as fluorescence targets. The red points in (a) depict the positions of the discrete point sources, located at z=2.2 cm. Tubes 1-5 in (b) depict the locations of five fluorescence targets in the phantom. Tube I and tube II in (b) depict the locations of the two 8.5 mm diameter cylinders which contain the more absorptive fluid.

C. PHANTOM EXPERIMENT

The phantom experiment was performed by the hybrid FMT/XCT imaging system (see Fig. 1). In the experiment, two transparent glass cylinders [outer diameter ∼8.5 mm, see the green cylinders of Fig. 3(a)] were placed into a larger transparent glass cylinder (outer diameter ∼3.0 cm) to produce heterogeneous phantom, as shown in Fig. 3. The background optical properties were assigned as $\mu_a = 0.3\ \text{cm}^{-1}$ and $\mu_s' = 10.0\ \text{cm}^{-1}$, similar to the bulk optical properties of mouse tissues. The optical properties $\mu_a = 1.0\ \text{cm}^{-1}$ and $\mu_s' = 10.0\ \text{cm}^{-1}$ were assigned to the two 8.5 mm diameter cylinders, in order to simulate the highly absorptive tissues of small animals (e.g., the liver). Five transparent glass tubes [outer diameter ∼4.5 mm, see Fig. 3(b)] filled with 1 μM ICG solution were immerged in the phantom, as fluorescence targets. The total excitation light power delivered on the phantom surface was about 3 mW.

For optical imaging, 24 fluorescence images and excitation light images were acquired every 15°. When collecting the fluorescence images, an 840±6nm band-pass filter (Semrock, Rochester, NY, USA) was placed in front of the EMCCD camera. When collecting the excitation light images, a neutral density filter (Daheng, Beijing, China) of 1% transmittance was used to prevent possible highlight damage to EMCCD. After fluorescence imaging, XCT was performed to obtain the structure information of the imaged object. In XCT scanning, the x-ray source voltage and current were set to 45kV and 1mA, respectively.

In this paper, the reconstructed slices of FMT and XCT were co-registered based on the axis of rotation. To provide the height information for co-registration, a steel anchor point, which could be imaged in both imaging systems, was plastered on the mouse surface. The detailed information for the registration could be found in our previous work [5].

IV. RESULTS

A. EVALUATING THE EFFECT OF STRUCTURAL A PRIORI INFORMATION ON FMT RECONSTRUCTION IN NUMERICAL SIMULATION

The *structural a priori* information is one of the important factors that affect the FMT reconstructions. To evaluate the effect, in the numerical simulation, the reconstructions were performed using respectively: (i) the Tikhonov regularization, (ii) the Laplace regularization, and (iii) the Laplace with weighted segments regularization. The standard Tikhonov regularization did not depend on *structural a priori* information, while both (ii) and (iii) were taking into account *structural a priori* information. Noted that the accurate optical properties (*functional a priori* information) was used in above all reconstructions.

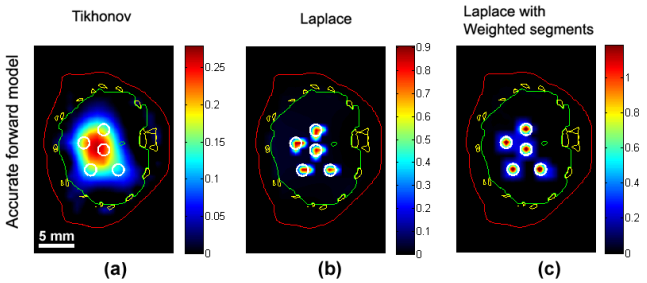

FIGURE 4. The reconstructed results (z=1.3 cm) obtained by different structural regularizations. (a) Tikhonov regularization. (b) Laplace regularization. (c) Laplace with weighted segments regularization. (a) does not include *structural a priori* information. Both (b) and (c) include *structural a priori* information acquired by the segmentation of XCT. Note that the accurate optical properties (*functional a priori* information) are used in all reconstructions. The actual boundaries of different organs are depicted with different colors (surface: red; liver: green; bones: yellow).

Fig. 4 depicts the tomographic images obtained with different structural regularizations. Fig. 4(a) shows the reconstructed result with standard Tikhonov regularization, which does not use *structural a priori* information. Figs. 4(b) and (c) show the reconstructed results obtained by the Laplace method and the Laplace with weighted segments method, where *structural a priori* information from the segmentation of XCT is used in reconstruction processes. In the case, *structural a priori* information used is the heart, lung, liver, spleen, stomach, bones, fluorescence inclusions, and other tissues.

The results suggest that even if the accurate optical properties are known, without *structural a priori* information, it is difficult to clearly localize the distributions of five fluorescence targets in the liver. In contrast, when *structural a priori* information is utilized to guide and constrain the FMT reconstruction process, the five fluorescence targets embedded in the liver can be localized accurately.

B. EVALUATING THE EFFECT OF FUNCTIONAL A PRIORI INFORMATION ON FMT RECONSTRUCTION IN NUMERICAL SIMULATION

As mentioned above, the reconstruction accuracy of FMT can be improved if *functional a priori* information is

used in reconstruction processes. Considering that there might be some extent of variances between the calculated and the true optical properties in experiments (especially in *in vivo* experiments), in this case, the optical properties with $\pm 10\% \sim \pm 50\%$ mismatch in μ_s' and μ_a and the homogeneous optical properties ($\mu_s' = 10.0\ \mathrm{cm}^{-1}$ and $\mu_a = 0.3\ \mathrm{cm}^{-1}$) were used to evaluate the effect of *functional a priori* information on FMT reconstruction. In reconstruction processes, the forward model was generated by assigning the above optical properties to the heart, the lungs, the liver, the spleen, the stomach, and the bone, respectively. Since the optimal reconstructed results could be obtained by the Laplace with weighted segments regularization [see Fig. 4(c)], here, the reconstructions were performed with the Laplace with weighted segments regularization method for all of the forward models.

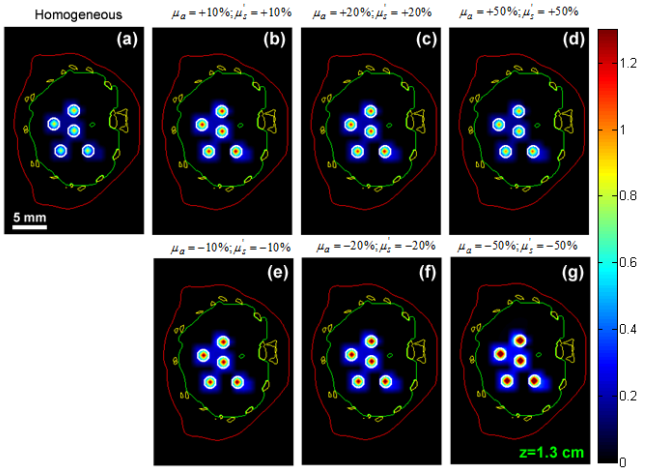

FIGURE 5. **The reconstructed results obtained using the Laplace with weighted segments regularization, incorporating homogeneous and mismatched optical properties. (a) The reconstructed results of the optical properties ($\mu_s' = 10.0\ \mathrm{cm}^{-1}$ and $\mu_a = 0.3\ \mathrm{cm}^{-1}$). (b) and (e) The reconstructed results of the heterogeneous optical properties with ±10% mismatch in μ_s' and μ_a. (c) and (f) The reconstructed results of the heterogeneous optical properties with ±20% mismatch in μ_s' and μ_a. (d) and (g) The reconstructed results of the heterogeneous optical properties with ±50% mismatch in μ_s' and μ_a. For all optical properties, reconstructions are performed with the Laplace with weighted segments regularization.**

Fig. 5 depicts the reconstructed results with different forward models. Fig. 5(a) shows the reconstructed result when a homogeneous model ($\mu_s' = 10.0\ \mathrm{cm}^{-1}$ and $\mu_a = 0.3\ \mathrm{cm}^{-1}$) is applied in reconstruction processes. Figs. 5(b)-(d) show the reconstructed results obtained when both μ_s' and μ_a increase by 10%, 20%, and 50%, respectively. Figs. 5(e)-(g) show the reconstructed results obtained when both μ_s' and μ_a decrease by 10%, 20%, and 50%, respectively. Further, the effect of *functional a priori* information on reconstruction accuracy is evaluated quantitatively through the relative error, summarized in Table 2.

The results suggest that the five fluorescence inclusions embedded in the liver can be correctly localized by using the Laplace with weighted segments regularization, even if there are great variances in the optical properties. However, it can also be found that the fluorophore concentration cannot be accurately recovered when the mismatched *functional a priori* information is used in reconstruction processes.

TABLE 2. **The relative errors in different tubes obtained by different forward models combined with the Laplace with weighted segments regularization (numerical simulation).**

Forward models	Relative Error				
	Tube 1	Tube 2	Tube 3	Tube 4	Tube 5
Homogeneous	27.01	23.40	29.27	28.14	25.32
Mis. +10%	4.34	3.75	4.48	3.90	3.60
Mis. +20%	8.42	7.18	8.63	7.51	6.96
Mis. +50%	19.67	16.43	19.91	17.53	16.44
Mis. -10%	4.72	4.20	4.91	4.32	3.98
Mis. -20%	9.97	9.04	10.41	9.26	8.52
Mis. -50%	32.44	31.62	34.02	31.71	29.64

C. EVALUATING THE EFFECT OF STRUCTURAL A PRIORI INFORMATION ON FMT RECONSTRUCTION IN PHANTOM EXPERIMENT

Similarly to the numerical simulation, in the phantom experiments, the Laplace regularization and the Laplace with weighted segments regularization, as structural regularization term, were used in reconstruction processes to evaluate the effect of *structural a priori* information on FMT reconstruction. Here, the *structural a priori* information used in the reconstruction was the tubes, the phantom, and other region.

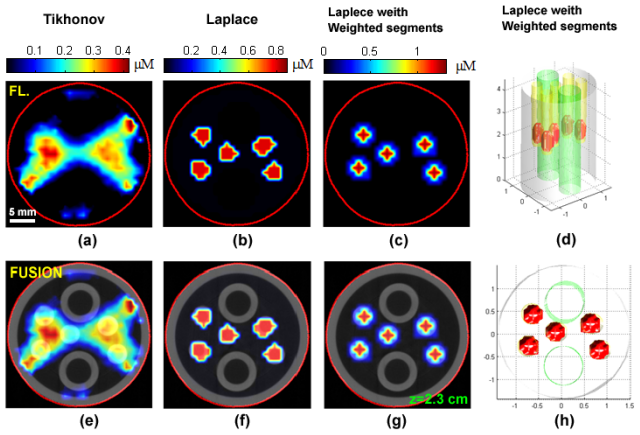

FIGURE 6. **The reconstructed results with different regularizations in phantom experiment. (a) Tikhonov regularization. (b) Laplace regularization. (c) Laplace with weighted segments regularization. (e), (f), and (g) The reconstructed fluorescence images overlaid onto the corresponding slices from XCT. The red curves in (a)-(c) and (e)-(g) depict the phantom boundary obtained by back-projecting the 72 white light images, which are used to further validate the accuracy of registration. (d) and (h) The 3-D rendering of the reconstructed images using different views. The red regions in (d) and (h) indicate the reconstructed ICG distributions, obtained by the Laplace with weighted segments regularization. Note that accurate optical properties are used in all reconstructions.**

Fig. 6 shows the reconstructed tomographic images, obtained by using different structural regularizations but incorporating accurate optical properties. Fig. 6(a) shows

the reconstructed result with the Tikhonov regularization. Figs. 6(b) and (c) show the reconstructed results using the Laplace method and Laplace with weighted segments method, respectively. The fusion results of FMT and XCT are shown in Figs. 6(e)-(g). Figs. 6(d) and (h) depict the 3-D rendering of the reconstructed images using different views. The red regions in Figs. 6(d) and (h) indicate the reconstructed ICG distributions, which are obtained by the Laplace with weighted segments regularization. As expected, the experimental results indicate that it is difficult to identify the location of five tubes in the phantom without *structural a priori* information. In contrast, when structure information is utilized to guide and constrain the FMT reconstruction, the five tubes can be correctly localized.

D. EVALUATING THE EFFECT OF FUNCTIONAL A PRIORI INFORMATION ON FMT RECONSTRUCTION IN PHANTOM EXPERIMENT

In the phantom experiments, we also constructed different forward models by various *functional a priori* information and evaluated their capability in FMT reconstruction. Similarly to the numerical simulation study, the optical properties with $\pm 10\%$, $\pm 20\%$, and $\pm 50\%$ mismatch in both μ_s' and μ_a and homogeneous model ($\mu_s' = 10.0\ \mathrm{cm}^{-1}$ and $\mu_a = 0.3\ \mathrm{cm}^{-1}$) were used to simulate the cases in *in vivo* application, where the optical properties might have a combination of positive and negative mismatch in μ_s' and μ_a. For all forward models, the reconstructions were performed with the Laplace with weighted segments regularization.

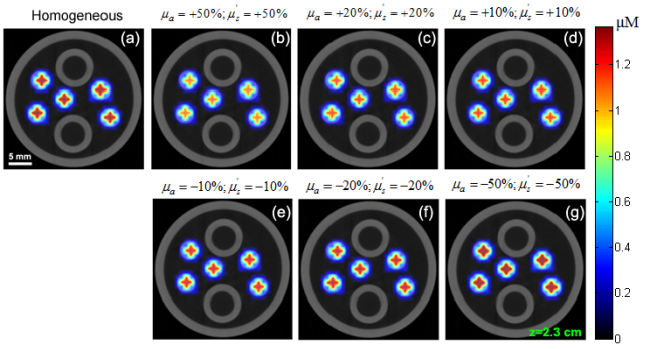

FIGURE 7. The reconstructed results obtained by the Laplace with weighted segments regularization, incorporating homogeneous and mismatch optical properties. (a) The reconstructed results of the homogeneous optical properties ($\mu_s' = 10.0\ \mathrm{cm}^{-1}$ and $\mu_a = 0.3\ \mathrm{cm}^{-1}$). (b)-(d) The reconstructed results of the heterogeneous optical properties with +50%, +20%, and +10% mismatch in μ_s' and μ_a. (e)-(g) The reconstructed results of the heterogeneous optical properties with −10%, −20%, and −50% mismatch in μ_s' and μ_a. For all optical properties, reconstructions are performed using the Laplace with weighted segments regularization.

Fig. 7 depicts the reconstructed results with different forward models. Fig. 7(a) shows the reconstructed result when the homogeneous model is applied. Figs. 7(b)-(d) show the reconstructed results obtained when both μ_s' and μ_a increase by 50%, 20%, and 10%, respectively. Figs. 7(e)-(g) show the reconstructed results obtained when both μ_s' and μ_a decrease by 10%, 20%, and 50%, respectively.

The results suggest that the five bubbles embedded in the phantom can be correctly localized using the Laplace with weighted segments regularization, even if there exists the variances in optical properties. However, similar to that indicated in the numerical simulation, the fluorophore concentration cannot be accurately recovered if accurate optical properties are not available (see Table 3).

TABLE 3. The relative errors in different tubes obtained by different forward models combined with the Laplace with weighted segments regularization (phantom experiment).

Forward models	Relative Error				
	Tube 1	Tube 2	Tube 3	Tube 4	Tube 5
Homogeneous	11.57	11.52	11.58	11.56	11.43
Mis. +10%	2.74	2.87	2.86	2.88	2.86
Mis. +20%	5.13	5.38	5.37	5.40	5.36
Mis. +50%	10.43	10.95	10.95	11.01	10.91
Mis. -10%	3.08	3.23	3.21	3.23	3.22
Mis. -20%	6.52	6.81	6.76	6.82	6.79
Mis. -50%	19.08	19.82	19.56	19.78	19.74

V. DISCUSSION AND CONCLUSION

Fluorescence molecular tomography plays an important role in biomedical research since it can non-invasive, quantitative, 3-D image the distribution of fluorophore in living subjects. However, FMT, as an imaging technique based on diffusive light, suffers from a low spatial resolution. In this paper, we have analyzed and compared the effect of *a priori* information, including *structural a priori* information (anatomical structure) and *functional a priori* information (optical properties of media/tissues), on the reconstruction accuracy of FMT.

As evident in the reconstructed results, even if the accurate forward model (*functional a priori* information) was used in FMT reconstruction processes, it was difficult to clearly localize the distributions of five inclusions embedded in the liver (simulation study) and in the phantom (phantom experiment), if *structural a priori* information was not taken into account [see Fig. 4(a) and Fig. 6(e)]. This was probably caused by the diffusive nature of photon migration in biological tissues and the ill-posed characteristic of the inverse problem. In contrast, when *structural a priori* information was utilized to guide and constrain the reconstruction process, as was done in the Laplace regularization and the Laplace with weighted segments regularization, the five fluorescence inclusions could be correctly localized [see Figs. 4(b) and (c), Figs. 6(f) and (g)]. Even when the variances in optical properties was significant, e.g., 50% overestimate and underestimate discrepancies in μ_s' and μ_a, the five fluorescence inclusions could still be localized if *structural a priori* information was available (see Figs. 5 and 7).

On the other hand, the simulation and experiment results also suggested that the *structural a priori* information alone was insufficient to recover fluorophore concentration, if *functional a priori* information were not taken into account. As demonstrated in the simulation study, the relative errors

in the fluorescence target 1 were 32.44% for the −50% mismatched model, 9.97% for the −20% mismatched model, and 27.01% for the homogeneous model, respectively (see Table 2). Similarly, in the phantom experiment, the relative errors in the fluorescence target 1 was 19.08% for the −50% mismatched model and 6.52% for the −20% mismatched model, respectively (see Table 3). It indicated that with increasing variances in μ_s' and μ_a, there was an increase in the relative errors resulting from improper forward models.

Based on these results, we believe that the use of *structural a priori* information could correctly resolve the locations of fluorescence targets embedded in heterogeneous medium, even if there are great variances in the optical properties. On the other hand, we also think that both *functional and structural a priori* information are essential for the recovery of fluorophore concentration. When *structural a priori* information is applied alone or incorporating mismatched *functional a priori* information, the fluorophore concentration cannot be accurately recovered.

It should be also noted that in this study, the forward model describing light propagation in heterogeneous medium is generated using the first-order diffusion approximation to the radiative transport equation. In some particular regions, such as low scattering or higher absorption tissues, the diffusion equation fails to work properly. Hence the radiative transport equation [29] or high order spherical harmonics method [30] should be considered to further improve the accuracy of forward model. In addition, we also admit that a thorough investigation of the achievable spatial resolution for reconstruction is not yet conducted in the work. Systematic studies in the field will be performed in our future work.

In conclusion, using numerical simulation and phantom experiments, we have analyzed and compared the effect of *structural and functional a priori* information on FMT reconstruction accuracy. This study will help us in better guiding the experimental design for the application of *a priori* information in FMT reconstruction. Future work will be focused on applying *a priori* information in improving FMT imaging performance *in vivo*.

APPENDIX

CALCULATION OF a_i

The voxel weights a_i are calculated by multiplying the weights factor w_m by the segmentation matrix $\mathbf{C}$

$$a_i = \sum_{i=1}^{m} c_{i,m} w_m \tag{13}$$

where $\mathbf{C} = (c_{i,m})$, with a size of $N_{voxels} \times N_{segments}$, is a segmentation matrix. $N_{segment}$ is the number of anatomical segments; $c_{i,m}$ is the volume percentage of voxel i that is contained in segmentation region m; The weight factor w_m is obtained by the following equation

$$w_m = \sqrt{\frac{(1+\beta)\max c}{c_m + \beta \max c}} \tag{14}$$

where the parameter β is set to 0.066 for all experiments according to [9]. c is a mean fluorescence intensity for each anatomical region, which is obtained by solving Eq. (15) with algebraic reconstruction technique (ART) with non-negative constraints

$$\tilde{\mathbf{W}} c = u \tag{15}$$

where $\tilde{\mathbf{W}} = \mathbf{WC}$, with a size of $N_{data} \times N_{segments}$ and u is the measured fluorescence signal.

ACKNOWLEDGMENT

The authors would like to acknowledge J. Bai for providing the imaging equipments.

REFERENCES

[1] V. Ntziachristos, J. Ripoll, L. V. Wang, and R. Weissleder, "Looking and listening to light: The evolution of whole-body photonic imaging," *Nature Biotechnol.*, vol. 23, pp. 313–320, Mar. 2005.

[2] R. Weissleder and V. Ntziachristos, "Shedding light onto live molecular targets," *Nature Med.*, vol. 9, no. 1, pp. 123–128, Jan. 2003.

[3] X. Gao, Y. Cui, R. M. Levenson, L. W. K. Chung, and S. Nie, "*In vivo* cancer targeting and imaging with semiconductor quantum dots," *Nature Biotechnol.*, vol. 22, pp. 969–976, Jul. 2004.

[4] X. Michalet *et al.*, "Quantum dots for live cells, *in vivo* imaging, and diagnostics," *Science*, vol. 307, no. 5709, pp. 538–544, 2005.

[5] X. Guo *et al.*, "A combined fluorescence and microcomputed tomography system for small animal imaging," *IEEE Trans. Biomed. Eng.*, vol. 57, no. 12, pp. 2876–2883, Dec. 2010.

[6] Y. Lin, W. C. Barber, J. S. Iwanczyk, W. Roeck, O. Nalcioglu, and G. Gulsen, "Quantitative fluorescence tomography using a combined tri-modality FT/DOT/XCT system," *Opt. Exp.*, vol. 18, no. 8, pp. 7835–7850, 2010.

[7] S. C. Davis *et al.*, "Magnetic resonance–coupled fluorescence tomography scanner for molecular imaging of tissue," *Rev. Sci. Instrum.*, vol. 79, no. 6, pp. 064302-1–064302-10, 2008.

[8] D. Hyde, E. L. Miller, D. H. Brooks, and V. Ntziachristos, "Data specific spatially varying regularization for multimodal fluorescence molecular tomography," *IEEE Trans. Med. Imag.*, vol. 29, no. 2, pp. 365–374, Feb. 2010.

[9] A. Ale, R. B. Schulz, A. Sarantopoulos, and V. Ntziachristos, "Imaging performance of a hybrid X-ray computed tomography-fluorescence molecular tomography system using priors," *Med. Phys.*, vol. 37, no. 5, pp. 1976–1986, 2010.

[10] D. Hyde, R. Schulz, D. Brooks, E. Miller, and V. Ntziachristos, "Performance dependence of hybrid X-ray computed tomography/fluorescence molecular tomography on the optical forward problem," *J. Opt. Soc. Amer. A*, vol. 26, no. 4, pp. 919–923, 2009.

[11] Y. Lin, W. C. Barber, J. S. Iwanczyk, W. W. Roeck, O. Nalcioglu, and G. Gulsena, "Quantitative fluorescence tomography using a tri-modality system: *In vivo* validation," *J. Biomed. Opt.*, vol. 15, no. 4, pp. 040503-1–040503-3, 2010.

[12] S. C. Davis, H. Dehghani, J. Wang, S. Jiang, B. W. Pogue, and K. D. Paulsen, "Image-guided diffuse optical fluorescence tomography implemented with Laplacian-type regularization," *Opt. Exp.*, vol. 15, no. 7, pp. 4066–4082, 2007.

[13] P. K. Yalavarthy, B. W. Pogue, H. Dehghani, C. M. Carpenter, S. Jiang, and K. D. Paulsen, "Structural information within regularization matrices improves near infrared diffuse optical tomography," *Opt. Exp.*, vol. 15, no. 13, pp. 8043–8058, 2007.

[14] Y. Tan and H. Jiang, "Diffuse optical tomography guided quantitative fluorescence molecular tomography," *Appl. Opt.*, vol. 47, no. 12, pp. 2011–2016, 2008.

[15] D. Wang, X. Liu, Y. Chen, and J. Bai, "A novel finite-element-based algorithm for fluorescence molecular tomography of heterogeneous media," *IEEE Trans. Inf. Technol. Biomed.*, vol. 13, no. 5, pp. 766–773, Sep. 2009.

[16] X. Liu, F. Liu, Y. Zhang, and J. Bai, "Unmixing dynamic fluorescence diffuse optical tomography images with independent component analysis," *IEEE Trans. Med. Imag.*, vol. 30, no. 9, pp. 1591–1604, Sep. 2011.

[17] V. Ntziachristos and R. Weissleder, "Experimental three-dimensional fluorescence reconstruction of diffuse media by use of a normalized Born approximation," *Opt. Lett.*, vol. 26, no. 12, pp. 893–895, 2001.
[18] M. A. O'Leary, D. A. Boas, X. D. Li, B. Chance, and A. G. Yodh, "Fluorescence lifetime imaging in turbid media," *Opt. Lett.*, vol. 21, no. 2, pp. 158–160, 1996.
[19] M. Schweiger, S. R. Arridge, M. Hiraoka, and D. T. Delpy, "The finite element method for the propagation of light in scattering media: Boundary and source conditions," *Med. Phys.*, vol. 22, no. 11, pp. 1779–1792, 1995.
[20] S. R. Arridge, M. Schweiger, M. Hiraoka, and D. T. Delpy, "A finite element approach for modeling photon transport in tissue," *Med. Phys.*, vol. 20, no. 2, pp. 299–309, 1993.
[21] S. C. Davis, K. S. Samkoe, J. A. O'Hara, S. L. Gibbs-Strauss, K. D. Paulsen, and B. W. Pogue, "Comparing implementations of magnetic-resonance-guided fluorescence molecular tomography for diagnostic classification of brain tumors," *J. Biomed. Opt.*, vol. 15, no. 5, pp. 051602-1–051602-10, 2010.
[22] D. Hyde *et al.*, "Hybrid FMT–CT imaging of amyloid-β plaques in a murine Alzheimer's disease model," *NeuroImage*, vol. 44, no. 4, pp. 1304–1311, 2009.
[23] X. Intes, J. Ripoll, Y. Chen, S. Nioka, A. G. Yodh, and B. Chance, "*In vivo* continuous-wave optical breast imaging enhanced with indocyanine green," *Med. Phys.*, vol. 30, no. 6, pp. 1039–1047, 2003.
[24] X. Liu *et al.*, "Imaging of indocyanine green perfusion in mouse liver with fluorescence diffuse optical tomography," *IEEE Trans. Biomed. Eng.*, vol. 58, no. 8, pp. 2139–2143, Aug. 2011.
[25] P. C. Hansen, "Analysis of discrete ill-posed problems by means of the L-curve," *SIAM Rev.*, vol. 34, no. 4, pp. 561–580, 1992.
[26] C. C. Paige and M. A. Saunders, "LSQR: An algorithm for sparse linear equations and sparse least squares," *ACM Trans. Math. Softw.*, vol. 8, no. 1, pp. 43–71, 1982.
[27] B. Dogdas, D. Stout, A. F. Chatziioannou, and R. M. Leahy, "Digimouse: A 3D whole body mouse atlas from CT and cryosection data," *Phys. Med. Biol.*, vol. 52, no. 3, pp. 577–587, 2007.
[28] G. Alexandrakis, F. R. Rannou, and A. F. Chatziioannou, "Tomographic bioluminescence imaging by use of a combined optical-PET (OPET) system: A computer simulation feasibility study," *Phys. Med. Biol.*, vol. 50, no. 17, pp. 4225–4241, 2005.
[29] Y. Lu, H. B. Machado, A. Douraghy, D. Stout, H. Herschman, and A. F. Chatziioannou, "Experimental bioluminescence tomography with fully parallel radiative-transfer-based reconstruction framework," *Opt. Exp.*, vol. 17, no. 19, pp. 16681–16695, 2009.
[30] A. D. Klose and E. W. Larsen, "Light transport in biological tissue based on the simplified spherical harmonics equations," *J. Comput. Phys.*, vol. 220, no. 1, pp. 441–470, 2006.

XIN LIU (S'09–M'12) received the bachelor's and master's degrees from Fourth Military Medical University, Xi'an, China, in 2001 and 2006, respectively, and the Ph.D. (Hons.) degree in biomedical engineering from Tsinghua University, Beijing, China, in 2012. From 2001 to 2014, he was an Assistant Professor with the Department of Biomedical Engineering, Fourth Military Medical University. He is currently with the School of Communication and Information Engineering, Shanghai University, Shanghai, China. He has published 21 papers, of which 12 are first-authored. He has co-authored two book chapters. His current research interests include fluorescence molecular tomography, super-resolution fluorescence microscopy, and X-ray luminescence/fluorescence computed tomography.

ZHUANGZHI YAN was born in 1961. He received the B.S. degree in automatic instrumentation from Tianjin University, Tianjin, China, in 1983, and the M.S. and Ph.D. degrees in electrical engineering from Kyoto University, Kyoto, Japan, in 1987 and 1993, respectively. He is currently a Professor and the Deputy Dean of the School of Communication and Information Engineering with Shanghai University. He serves as the Director of the Shanghai Institute of Biomedical Engineering. He has authored many papers in journals and conferences worldwide. His research interests include biomedical imaging and image analysis, computer aided diagnosis in medicine, and biomedical instrumentation. He serves as an Associate Editor of the *Journal of Applied Science* and the *Chinese Journal of Medical Instrumentation*.

HONGBING LU (M'00) received the Ph.D. degree in biomedical engineering from Tsinghua University, Beijing, China, in 1998. She was a Post-Doctoral Researcher in Radiology with the State University of New York at Stony Brook for three years. She joined Fourth Military Medical University in 1991, where she is currently a Professor and the Director of the Medical Imaging and Intelligent Processing Laboratory with the School of Biomedical Engineering. She is a Principal Investigator of over 10 projects funded by the National Science Foundation of China, the Ministry of Science and Technology, and the Department of Defense. She has authored over 90 journal publications. Her research interests focus on quantitative reconstruction of computed tomography, low-dose computed tomography imaging, computer-aided detection and diagnosis, and brain imaging and analysis. She is also an Associate Editor of the IEEE TRANSACTIONS ON MEDICAL IMAGING.